1   **A minimal synaptic model for direction selective neurons in *Drosophila***

2

3   Jacob A. Zavatone-Veth[1,2,a], Bara A. Badwan[3], Damon A. Clark[1,2,4,5,#]

4   1 – Department of Physics

5   2 – Department of Molecular, Cellular, and Developmental Biology

6   3 – School of Engineering and Applied Science

7   4 – Interdepartmental Neuroscience Program

8   5 – Department of Neuroscience

9   Yale University, New Haven, CT 06511, USA

10

11   a – Present address: Department of Physics, Harvard University, Cambridge, MA 02138, USA

12   # – Corresponding author

13

14   **Abstract**

15

16   Visual motion estimation is a canonical neural computation. In *Drosophila*, recent advances have

17   identified anatomical and functional circuitry underlying direction-selective computations.

18   Models with varying levels of abstraction have been proposed to explain specific experimental

19   results, but have rarely been compared across experiments. Here we construct a minimal,

20   biophysically inspired synaptic model for *Drosophila*'s first-order direction-selective T4 cells

21   using the wealth of available anatomical and physiological data. We show how this model relates

22   mathematically to classical models of motion detection, including the Hassenstein-Reichardt

23   correlator model. We used numerical simulation to test how well this synaptic model could

24   reproduce measurements of T4 cells across many datasets and stimulus modalities. These

25   comparisons include responses to sinusoid gratings, to apparent motion stimuli, to stochastic

26   stimuli, and to natural scenes. Without fine-tuning this model, it sufficed to reproduce many, but

27   not all, response properties of T4 cells. Since this model is flexible and based on straightforward

28   biophysical properties, it provides an extensible framework for developing a mechanistic

29   understanding of T4 neural response properties. Moreover, it can be used to assess the

30   sufficiency of simple biophysical mechanisms to describe features of the direction-selective

31   computation and identify where our understanding must be improved.

32

Introduction

34

35   Motion estimation is a canonical visual computation that requires integrating information

36   nonlinearly over both time and space. Direction-selective signals are tuned to motion in a

37   preferred-direction (PD), which elicits the strongest responses, while motion in the opposite,

38   null-direction (ND), elicits a weaker response. This directional computation has been described

39   by a wide variety of computational models. Classical models, such as the Hassenstein-Reichardt

40   correlator (HRC) (Hassenstein and Reichardt, 1956) and motion energy model (Adelson and

41   Bergen, 1985), rely on sensing correlations between pairs points separated in time and space.

42   These phenomenological models have provided striking insights into neural and behavioral

43   responses in a variety of species, including in flies (Yang and Clandinin, 2018).

44

45   In the last decade, advances in defining the anatomical and functional connectivity of

46   *Drosophila*'s visual circuits suggest that we should move towards more mechanistic, biophysical

47   descriptions of this computation. Here, we follow previous work (Gruntman et al., 2018; Torre

48   and Poggio, 1978) to propose a simple, biophysically-plausible synaptic model for direction-

49   selectivity in Drosophila's ON-edge sensitive motion pathway. We compare its predictions to

50   measurements made by several research groups in response to many stimuli, giving us a tool for

51   understanding which features are sufficient to describe different response properties.

52

53   The inputs to direction-selective cells have been identified by electron microscopy and through

54   genetic silencing experiments. The most peripheral direction-selective neurons in the *Drosophila*

55   optic lobe are the T4 and T5 cells, which are sensitive to moving ON-edges (consisting of

56   contrast increments) and OFF-edges (consisting of contrast decrements), respectively (Clark et

57   al., 2011; Joesch et al., 2010; Maisak et al., 2013). Electron microscopy and genetic silencing

58   have identified primary inputs to T4 and T5 cells (Serbe et al., 2016; Shinomiya et al., 2019;

59   Strother et al., 2017; Takemura et al., 2017). These studies suggest that T4 cells receive input

60   from three distinct colinear spatial locations, with the neurons Mi1 and Tm3 both relaying

61   information about the central point, and the neurons Mi9 and Mi4 acting as relays for the two

62   flanking points (Takemura et al., 2017) (**Fig. 1A**). The neuron T5 appears to have a similar

63   spatial structure, with different input neurons (Shinomiya et al., 2019). Both cell types also

64   receive spatially-localized inputs from other neurons, whose functions remain less well

65   understood (Shinomiya et al., 2019; Takemura et al., 2017).

66

67   The physiological properties of the inputs to T4 and T5 cells have also been characterized. At

68   their receptive field centers, Mi1 and Tm3 cells respond quickly to visual stimuli, and provide

69   excitatory input to T4 (Arenz et al., 2017; Behnia et al., 2014; Gruntman et al., 2018; Strother et

70   al., 2017; Takemura et al., 2017). On the preferred direction side of the receptive field, the cells

71   Mi4 and CT1 are ON cells with slower kinetics, likely inhibiting T4 cells (Arenz et al., 2017;

72   Shinomiya et al., 2019; Takemura et al., 2017). On the null direction side of the receptive field,

73   Mi9 cells are delayed OFF cells, which are likely to provide inhibitory, glutamatergic input to T4

74   cells (Arenz et al., 2017; Salazar-Gatzimas et al., 2018). The inputs to T5 cells similarly appear

75   to be arranged with a fast central input and delayed flanking inputs, but whether these inputs

76   excite or inhibit T5 is less clear (Arenz et al., 2017; Behnia et al., 2014; Shinomiya et al., 2019;

77   Wienecke et al., 2018).

78

79   The functional properties of the T4 and T5 cells and their inputs have been interrogated using

80   many stimulus and measurement modalities. This wealth of data has led to many different

81   models that seek to describe the response properties of T4 and T5 cells (Arenz et al., 2017;

82   Badwan et al., 2019; Behnia et al., 2014; Clark et al., 2011; Creamer et al., 2018; Eichner et al.,

83   2011; Gruntman et al., 2018; Haag et al., 2016; Leong et al., 2016; Leonhardt et al., 2016;

84   Salazar-Gatzimas et al., 2018; Salazar-Gatzimas et al., 2016; Serbe et al., 2016; Strother et al.,

85   2017; Wienecke et al., 2018). Many measurements of T4 and T5 have demonstrated

86   phenomenology that could not be produced by the classical HRC model. However, proposed

87   models were most often evaluated by how they reproduced the associated dataset, rather than the

88   full the range of phenomena in the literature. Here we ask how a minimal, constrained model

89   reproduces T4 phenomenology (and some T5 phenomenology) from many different experiments.

90   We compare the model to data in response to moving edges, to sinusoids, to apparent motion

91   stimuli, to stochastic stimuli, and to natural scenes.

92

93   In this minimal model, the spatially-separated inputs to T4 are represented as three linear-

94   nonlinear (LN) transformations of the input contrast (Dayan and Abbott, 2001). These model

95   neurons then interact with T4 by altering the conductance of excitatory and inhibitory currents

96   (Gruntman et al., 2018; Torre and Poggio, 1978). This construction is simple enough to allow

97   some algorithmic intuition but incorporates greater biophysical realism than most

98   phenomenological models. We do not fit the model to every dataset. Rather, our goal is to test

99   the sufficiency of a minimal circuit model to account for different measured phenomena in T4

100   cells. This model does not contain any exotic channels or receptors, and it biophysically models

101   the membrane voltage and intracellular calcium concentration in T4 neurons. It does not

102   reproduce all functional properties of T4 cells, but it provides a flexible framework for

103   understanding the sufficiency of simple circuit properties and mechanisms to describe the

104   processing properties of T4 neurons. In cases where this model is insufficient to describe data,

105   we suggest how model parameters might be changed to better describe the data.

106

107   **Methods**

108

109   *Constructing an anatomically constrained synaptic model for T4 cells*

110   Following proposed synaptic architectures for direction-selective computations (Gruntman et al.,

111   2018; Torre and Poggio, 1978), we constructed an elementary motion detector based on the

112   connectome of the *Drosophila* optic lobe. We simplified this structure to consider three inputs to

113   a T4 cell: a delayed ND-offset OFF inhibitory input representing Mi9, a centered ON excitatory

114   input representing Mi1 and Tm3, and a delayed PD-offset ON inhibitory input representing Mi4

115   (and/or CT1) (**Figure 1A**) (Strother et al., 2017; Takemura et al., 2017).

116

117   We will model these inputs to T4 cells as simple linear-nonlinear (LN) transformations of the

118   input contrast (Behnia et al., 2014). We will further model effects of these synaptic inputs on the

119   membrane potential of the T4 cell by changes in the conductance of excitatory and inhibitory

120   currents (Torre and Poggio, 1978). For notational convenience, we define our model below in

121   continuous space and time, noting as needed where adjustments are made for the discretization

122   used in numerical simulation. We take the inputs to the model to be contrasts. We take each

123   input to the motion detector to have an L_1-normalized Gaussian spatial acceptance function

124

$$h(x) = \frac{1}{\sqrt{2\pi\sigma^2}} \, e^{-\frac{x^2}{2\sigma^2}}$$

126

127   where the spatial parameter σ is related to the full width at half maximum (FWHM) of the

128   acceptance function by FWHM $= 2\sqrt{2\log 2}\,\sigma$. We fix FWHM $= 5.7°$ to approximately match

129   the spatial acceptance functions of photoreceptors in the fly eye (Stavenga, 2003). To represent

130   the delayed inputs to the motion detector, we use the L_2-normalized lowpass temporal filter

131

$$f(t) = 2\,\tau^{-\frac{3}{2}}\,t\,\Theta(t)\,e^{-\frac{t}{\tau}}$$

133

134   where $\Theta(x)$ is the Heaviside step function. To represent the non-delayed central input to the

135   motion detector, we replace the temporal filter f by its derivative $\dot{f}$. We note that the term

136   resulting from the distributional derivative of $\Theta(t)$ vanishes when $\dot{f}$ is convolved with any signal

137   as it is proportional to $t\,\delta(t)$, where $\delta(x)$ is the Dirac delta distribution. Using these filters, we

138   define the filtered contrast signal s at each point in spacetime:

139

$$s(t, x) := (fh * c)(t, x)$$

141

142   where $c(t, x)$ is the input contrast and $*$ denotes spatiotemporal convolution over the appropriate

143   domain. As taking the temporal derivative of the filtered contrast signal is equivalent to filtering

144   with the derivative of the temporal filter, we will use the notation $\dot{s}$ for the high-pass-filtered

145   signal throughout. For convenient handling of spatial boundary conditions, we numerically

146   simulate the full 360° of visual space, which is a periodic interval.

147

148   We denote the spacing between neighboring inputs as Δ. Here, we use 5° spacing so that the

149   inputs evenly tile 360° of visual space. Then, we define the three inputs to the motion detector as

150   rectified-linear functions of the filtered contrast signal at three points in space, mimicking the

151   polarity-selectivity of the inputs to T4 cells:

152

153
$$g_1(t, x) := g_{\mathrm{inh}}\, R\big(-s(t, x - \Delta)\big)$$

154
$$g_2(t, x) := g_{\mathrm{exc}}\, R\big(\dot{s}(t, x)\big)$$

155
$$g_3(t, x) := g_{\mathrm{inh}}\, R\big(s(t, x + \Delta)\big)$$

156

157 where $R(x) := \max\{0, x\}$ is the ramp function and g_{inh} and g_{exc} are parameters scaling the

158 effects of each input on the postsynaptic conductances (**Figure 1A-B**). Thus far, we have

159 represented the conductances as linear-nonlinear (LN) transformations of the input contrast

160 (Dayan and Abbott, 2001).

161

162 We define the membrane potential V_{m} of the postsynaptic cell such that the reversal potential for

163 leak currents is 0 mV. The cell's membrane voltage dynamics are then given as (Torre and

164 Poggio, 1978)

165

166
$$c_{\mathrm{m}}\dot{V}_{\mathrm{m}} + V_{\mathrm{m}}(g_{\mathrm{leak}} + g_1 + g_2 + g_3) = g_1 E_{\mathrm{inh}} + g_2 E_{\mathrm{exc}} + g_3 E_{\mathrm{inh}}$$

167

168 where c_{m} is the membrane capacitance, g_{leak} is the leak conductance, and E_{inh} and E_{exc} are the

169 reversal potentials for inhibitory and excitatory currents, respectively. Neglecting capacitive

170 currents, we solve for the pseudo-steady-state (Gruntman et al., 2018; Torre and Poggio, 1978).

171

172
$$V_{\mathrm{m}} = \frac{g_1 E_{\mathrm{inh}} + g_2 E_{\mathrm{exc}} + g_3 E_{\mathrm{inh}}}{g_{\mathrm{leak}} + g_1 + g_2 + g_3}$$

173

174 Then, we model the transformation from membrane voltage to calcium concentration C as a

175 positively rectifying half-quadratic function $R^2(x) := (R(x))^2$:

176

177
$$C(t, x) := R^2\big(V_{\mathrm{m}}(t, x)\big)$$

178

179 which qualitatively captures the expansive nonlinear effect of the transformation between

180 voltage and calcium (Kato et al., 2014; Leong et al., 2016) (**Figure 1B**).

181

182   *Visual stimuli*

183   We presented this model with spatiotemporal contrast patterns to mimic a variety of visual

184   stimuli used in the field. Detailed mathematical descriptions of each stimulus are given in

185   **Appendix A**. Briefly, we presented the model with moving and stationary sinusoidal gratings,

186   with apparent motion stimuli, with stochastic stimuli including those with imposed correlations,

187   and with natural scenes. In each case, we compared how the model responds to the published

188   responses of T4 and T5 neurons.

189

190   *Selecting model parameters*

191   This model uses a parameter set equal to one that was developed to explain direction-opponency

192   in T4 cells (Badwan et al., 2019). There, we fixed the filter time constant $\tau = 150$ ms to produce

193   peak responses to PD sinusoidal gratings at ~1 Hz (Badwan et al., 2019; Creamer et al., 2018;

194   Maisak et al., 2013). We fix the excitatory and inhibitory reversal potentials to values of $E_{\mathrm{exc}} =$

195   60 mV and $E_{\mathrm{inh}} = -30$ mV, which are plausible based on electrophysiological experiments

196   (Gruntman et al., 2018). As the model membrane potential can be rewritten as

197

198
$$V_{\mathrm{m}} = \left(\frac{g_1}{g_{\mathrm{leak}}} E_{\mathrm{inh}} + \frac{g_2}{g_{\mathrm{leak}}} E_{\mathrm{exc}} + \frac{g_3}{g_{\mathrm{leak}}} E_{\mathrm{inh}} \right) \left(1 + \frac{g_1}{g_{\mathrm{leak}}} + \frac{g_2}{g_{\mathrm{leak}}} + \frac{g_3}{g_{\mathrm{leak}}} \right)^{-1}$$

199

200   only the ratios of g_1, g_2, and g_3 to g_{leak}, rather than their absolute magnitudes, are relevant. We

201   therefore express the postsynaptic conductances as non-dimensional quantities in units of g_{leak},

202   leaving $g_{\mathrm{exc}}/g_{\mathrm{leak}}$ and $g_{\mathrm{inh}}/g_{\mathrm{leak}}$ as the model's two free parameters. The procedure used to

203   select the values of these parameters is described in detail in **Appendix B**. As shown previously

204   (Badwan et al., 2019), there exists a broad region of parameter space for which this model

205   displays responses to sinusoid gratings with a temporal frequency of 1 Hz and a spatial

206   wavelength of 45° consistent with those measured in T4 and T5 cells. We note that our choice of

207   filter normalization, which differs from that in the previous use of this model (Badwan et al.,

208   2019), affects the parameter values chosen, as it scales g_1, g_2, and g_3 relative to g_{leak}. **Table 1**

209   summarizes the model parameter values used in all simulations.

210

211   **Table 1:** Parameter values used in all simulations.

Parameter	Value
Photoreceptor spacing Δ	$5°$
Photoreceptor spatial FWHM	$5.7°$
Temporal filter time constant τ	0.150 s
Spatial sampling interval Δx	$0.5°$
Temporal sampling interval Δt	$1/240$ s
Leak current reversal potential E_{leak}	0 mV
Excitatory current reversal potential E_{exc}	$+60$ mV
Inhibitory current reversal potential E_{inh}	-30 mV
Excitatory to leak conductance ratio $g_{\text{exc}}/g_{\text{leak}}$	0.1
Inhibitory to leak conductance ratio $g_{\text{inh}}/g_{\text{leak}}$	0.3

212

213   In vivo *two-photon calcium imaging in T4 cells*

214   Most of our comparisons relate the synaptic model's responses to published data, but we also

215   compare the model to a new dataset of T4 cell responses to glider stimuli. The protocol for two-

216   photon calcium imaging in T4 cells matches published methods (Badwan et al., 2019) and used

217   Psychtoolbox (Brainard, 1997; Kleiner et al., 2007; Pelli, 1997) to present stimuli on a

218   panoramic visual display (Creamer et al., 2019). The glider stimuli presented during these

219   measurements are described in **Appendix A**. Net responses were computed as the difference in

220   responses to stimuli moving in the preferred and null directions of each T4 region of interest, and

221   then averaged within each fly. Non-parametric two-sided Wilcoxon signed-rank tests were used

222   to test whether median net responses differed significantly from zero (Hollander et al., 2013).

223   For statistical purposes, each individual fly was considered to be an independent sample.

224

225   *Numerical methods*

226   Numerical simulations were conducted using Matlab 9.6 (R2019a) (The MathWorks, Natick,

227   MA, USA). For stimuli containing randomly-generated components, responses were averaged

228 over 1000 realizations, and bootstrapped 95% confidence intervals for the mean were computed

229 using the bias-corrected and accelerated percentile method (Efron, 1987). **Results**

230

231 *The synaptic model reduces to HRC-like terms*

232 To gain intuition about the operation of the T4 synaptic model, we consider its expansion in the

233 small-input limit. To do so, we approximate the ramp function nonlinearity with a smooth

234 function that represents a soft rectifier, which can be approximated by a linear function for small

235 inputs (Fitzgerald and Clark, 2015). In particular, letting $s_1(t) := s(t, x - \Delta)$, $s_2(t) := s(t, x)$,

236 and $s_3(t) := s(t, x + \Delta)$, and defining the non-negative constants $\alpha := |g_{inh}E_{inh}/g_{leak}|$ and $\gamma :=$

237 $|g_{exc}E_{exc}/g_{leak}|$, we have, to lowest order in the inputs,

238

$$C \approx \frac{1}{16}(\alpha s_1 + \gamma \dot{s}_2 - \alpha s_3)^2$$

240

241 which may be rewritten as

242

$$C \approx \frac{\alpha^2}{16}(s_1 - s_3)^2 + \frac{\gamma^2}{16}(\dot{s}_2)^2 + \frac{\alpha\gamma}{8}(s_1\dot{s}_2 - \dot{s}_2 s_3)$$

244

245 This expansion represents a motion-energy approximation of the model. The first term in this

246 expansion is a finite-difference approximation to a spatial derivative, while the second term is a

247 temporal derivative at the center of the model's receptive field. The third term, which is the only

248 direction-selective term, is the subtraction of two offset correlators with opposite directional

249 tuning. This subtraction step provides some intuition for why this model mimics some properties

250 of a fully-opponent HRC model (Badwan et al., 2019). This same direction-selective term also

251 appears in the second-order expansion of the membrane voltage. Because this expansion of the

252 model is only to second-order, it is invariant under contrast inversions, and cannot account for

253 properties like ON-edge selectivity (Clark et al., 2014; Fitzgerald and Clark, 2015; Fitzgerald et

254 al., 2011). Though this simple description does not capture all properties of the synaptic model, it

255 provides intuition for the sensitivity of the model to certain stimulus features.

256

257 *The synaptic model is strongly ON/OFF-edge- and direction-selective*

258 T4 and T5 neurons are distinguished by the fact that T4 cells respond to ON-edges while T5 cells

259 respond to OFF-edges (Maisak et al., 2013). We first compared the ON/OFF edge- and direction-

260 selectivity of our T4 synaptic model to responses measured using two-photon calcium imaging in

261 T4 cells sensitive to front-to-back (FTB) motion. Like T4 FTB cells, our synaptic model

262 responded strongly to an ON edge moving in the FTB direction, but displayed little or no

263 response to OFF edges moving in the FTB direction or to edges of either polarity moving in the

264 back-to-front (BTF) direction (**Figure 1C**) (Maisak et al., 2013; Salazar-Gatzimas et al., 2016).

265

266 *The spatiotemporal tuning of the synaptic model is consistent with that of T4 cells*

267 Sinusoid grating stimuli are a common tool for characterizing direction-selective computations.

268 Responses to these stimuli have been used to suggest that the membrane voltage of T5 cells is a

269 nearly linear transformation of the visual input (**Figure 2A**) (Wienecke et al., 2018). In the

270 synaptic model, the membrane voltage is a nonlinear function of the input contrast because the

271 inputs are first rectified and then interact nonlinearly. We applied the same linearity testing

272 protocol to our model membrane voltage, constructing predictions for responses to PD and ND

273 drifting gratings from the responses to counterphase gratings (see **Appendix A**) (Jagadeesh et al.,

274 1993; Wienecke et al., 2018). The responses of the T4 synaptic model to drifting gratings were

275 similar to those predicted by a linear model for membrane voltage (**Figure 2A**). Thus, even a

276 nonlinear system like the T4 synaptic model may appear reasonably linear by this protocol.

277

278 T4 and T5 cells display direction-opponent average calcium responses to sinusoid gratings

279 (**Figure 2B**) (Badwan et al., 2019). This property means that the average response to PD motion

280 is reduced by the addition of ND motion, imposing a strong constraint on models for the

281 direction-selective computation. In particular, it implies that linear-nonlinear models with

282 expansive nonlinearities cannot account for the response properties of these cells (Badwan et al.,

283 2019). A variant of this synaptic model was proposed to account for these direction-opponent

284 responses (Badwan et al., 2019). This model reproduces the strong suppression when ND motion

285 is added to PD motion without substantial enhancement when orthogonal-direction (OD) motion

286 is added to PD motion (**Figure 2B**).

287

288   T4 and T5 cells are tuned to the temporal frequency of sinusoidal stimuli (**Figure 2C**) (Creamer

289   et al., 2018). This means that the mean neural response is maximal at a single temporal

290   frequency, independent of the wavelength. This property also applies to measurements of fly

291   behavior (Creamer et al., 2018; Kunze, 1961) and is consistent with the classical, fully-opponent

292   HRC. We presented the T4 synaptic model with drifting gratings of different spatial and

293   temporal frequencies to find the mean response to each. The model response was strongly

294   temporal-frequency-tuned (**Figure 2C**). To quantify the temporal-frequency-tuning, we asked

295   how much of the variance in this surface was accounted for by the product of one function of

296   temporal frequency and one fuction of spatial frequency response (Creamer et al., 2018; Priebe et

297   al., 2006). Such a separable model accounted for 99% of the variance in the response (see

298   **Appendix A**, **Figure 2C**). Because of our choice of parameters, the input temporal filters in this

299   model produce peak responses at around 1 Hz, lower than the roughly 2-4 Hz peak measured in

300   these T4 cells.

301

302   T4 and T5 cells respond to static gratings with amplitudes that depend on the grating orientation

303   (Fisher et al., 2015) (**Figure 2D**). The preferred orientation (defined by the vector normal to the

304   edges in a static grating) approximately matches the preferred direction of motion of these cells

305   (Maisak et al., 2013). The convention we use here for defining the orientation of a static grating

306   is rotated 90º relative to that used in the original study, which defined orientation in terms of

307   vectors parallel, rather than normal, to the edges (Fisher et al., 2015) (see **Appendix A**). When

308   the T4 synaptic model was presented with both static and drifting gratings of many different

309   orientations, it reproduced the orientation tuning observed experimentally for both static and

310   moving gratings (**Figure 2D**). The model was more selective for both orientation and direction

311   than the T4 cell measurements.

312

313   *The synaptic model reproduces the selectivity of apparent motion responses in T4 cells*

314   In addition to sinusoid gratings, apparent motion stimuli are a useful tool for investigating

315   direction-selective systems. These stimuli decompose visual motion into summations of simpler

316   spatiotemporal patterns, which can provide strong intuition into the motion computation (Barlow

317   and Levick, 1965).

318

11

319 Electrophysiological measurements of T4 cells have shown fast depolarization and delayed,

320 offset hyperpolarization in response to a small flashed white bar placed on a gray background

321 (Gruntman et al., 2018) (**Figure 3A**). The synaptic T4 model displayed qualitatively consistent

322 responses to the same stimulus (**Figure 3A**). The positive lobe in the model is narrower than in

323 the electrophysiological recording; this is likely because the true central input to T4 has a wider

324 receptive field than in our model (Behnia et al., 2014; Takemura et al., 2013). Consistent with

325 electrophysiology, the OFF input to the T4 model is not visible under this analysis because it was

326 rectified with a threshold at mean gray (zero contrast).

327

328 Since the synaptic model reproduced T4 cell voltage responses to flashed bars, we sought to

329 characterize its responses to apparent motion stimuli composed of pairs of bars offset in

330 spacetime (Salazar-Gatzimas et al., 2018). These stimuli can induce in humans and in flies the

331 "reverse-phi" motion illusion, in which a reversal of contrast polarity induces a motion percept in

332 the direction opposite the stimulus displacement (Anstis, 1970; Clark et al., 2011; Hassenstein

333 and Reichardt, 1956). We aligned these stimuli so that the temporally-delayed bar is placed at the

334 center of the receptive field (**Figure 3B**) (Salazar-Gatzimas et al., 2018). T4 cells respond

335 maximally to one phi and one reverse-phi apparent motion stimulus out of eight possible pairings

336 (Salazar-Gatzimas et al., 2018). The synaptic model reproduced this selectivity (**Figure 3C-D**).

337

338 Various groups have assessed nonlinear enhancement or suppression of PD and ND apparent

339 motion stimuli relative to linear decompositions. This analysis can be misleading because it does

340 not allow one to uniquely characterize the nonlinearity as 'enhancing' or 'suppressing', since

341 there exist an infinite number of linear decompositions of a given stimulus (Salazar-Gatzimas et

342 al., 2018). Despite this difficulty, such analyses have been applied as an intuitive way to try to

343 understand direction-selective computations (Barlow and Levick, 1965; Fisher et al., 2015;

344 Gruntman et al., 2018; Haag et al., 2016).

345

346 In T4 cells, an analysis of responses to sequential bars has indicated that calcium signals include

347 both PD enhancement and ND suppression relative to a linear prediction from the responses to

348 individual bars (Haag et al., 2016) (**Figure 3E**). Our model failed to reproduce this result,

349 showing only suppression of ND motion under this analysis (**Figure 3E**). This discrepancy could

350   be influenced by the timescale of this stimulus, which is far longer than the 150 ms offset used in

351   the apparent motion stimuli in (**Figure 3C-D**). Additionally, previous theoretical work has

352   shown that disinhibition can generate PD enhancement in similar models (Borst, 2018; Torre and

353   Poggio, 1978); the choice of thresholds in this model did not permit flanking disinhibition with

354   ON stimuli.

355

356   *The synaptic model does not reproduce the fast timescale tuning of T4 cells*

357   A third approach to characterizing direction-selective signals has been to apply stochastic stimuli

358   with specified correlation structure. Responses to uncorrelated stimuli can be used to generate an

359   unbiased estimate of a system's linear receptive field (Chichilnisky, 2001). By using reverse-

360   correlation and uncorrelated stimuli to extract spatiotemporal receptive fields, T4 cells have been

361   characterized by oriented linear receptive fields with a central excitatory lobe and a delayed,

362   offset inhibitory lobe (**Figure 4A**) (Leong et al., 2016; Salazar-Gatzimas et al., 2016). The T4

363   synaptic model generates the same shape of receptive field (**Figure 4A**). However, in the model,

364   the inhibitory lobe lasts longer than that measured in T4 cells, and the tuning of the model was

365   slower overall.

366

367   Responses to stochastic stimuli containing precise pairwise spatiotemporal correlations have

368   revealed fast-timescale tuning in T4 cells (Salazar-Gatzimas et al., 2016). In measurements of T4

369   and T5, the cells could discriminate between spatiotemporal correlations with delays of 0 and 15

370   ms (**Figure 4B**). We presented the synaptic model with stimuli containing pairwise

371   spatiotemporal correlations at different temporal delays. The model was direction-selective and

372   responded to both positive and negative correlations, as in the cellular measurements. However,

373   the model did not reproduce the fast timescale discrimination between delays (**Figure 4B**).

374   Furthermore, the synaptic model showed strong suppression of ND-oriented positive correlations

375   and enhancement of ND-oriented negative correlations, which was not observed in the data.

376

377   Behaving *Drosophila* respond direction-selectively to correlations higher than second-order

378   (Clark et al., 2014; Leonhardt et al., 2016). This cannot be explained by models that compute

379   pairwise correlations in the stimulus, such as the HRC and motion energy model. The sensitivity

380   to higher-order correlations has been assessed using three-point glider stimuli, which contain

381   precise third-order correlations (Hu and Victor, 2010) (**Figure 4C**). The net responses of T4 cells

382   to these stimuli have previously been inferred from behavioral measurements in *Drosophila* with

383   the synaptic outputs of T5 cells silenced, using gliders updated at 24 Hz (Leonhardt et al., 2016).

384   We used *in vivo* two-photon calcium imaging to measure directly the responses of T4 cells to

385   three-point gliders updated at 5 Hz, and found that the signs of the net responses were consistent

386   with those measured in behavior with T5 cells silenced (**Figure 4C**, see **Methods** and **Appendix**

387   **A** for details).

388

389   With an update rate of 24 Hz, the synaptic model correctly predicted the signs of net responses to

390   diverging gliders measured in imaging and behavior, but predicted the wrong converging glider

391   responses (**Figure 4C**). At 5 Hz, the synaptic model correctly predicted the signs of both

392   converging and diverging glider responses, but not the relative magnitudes. Thus, the glider

393   responses in T4 appear relatively insensitive to the glider timescale (24 vs. 5 Hz), but the

394   model's response depends strongly on the input timescales.

395

396   T4 and T5 cells have been shown to display strongly direction-selective responses to rigidly-

397   translating stimuli consisting of black and white squares placed at random on a gray background

398   (see **Appendix A**) (Badwan et al., 2019). When two such stimuli that move in opposite

399   directions are superimposed, they generate transparent motion percepts in primates (Qian et al.,

400   1994), and they generate responses in T4 that are reduced compared to presenting PD stimuli

401   alone (Badwan et al., 2019). The synaptic model qualitatively reproduced these responses

402   (**Figure 4D**). In particular, the responses of T4 cells are suppressed more strongly under the

403   addition of ND motion than under the addition of OD motion, a feature that is reproduced by the

404   synaptic T4 model (**Figure 4D**). Therefore, as in T4 cells, the selective direction-opponency

405   observed in the model persists even with stimuli containing multiple spatiotemporal frequencies.

406

407   *The T4 synaptic model provides decorrelated channels for naturalistic motion*

408   Beyond artificial stimuli, natural scenes have been used to investigate the performance of

409   direction-selective signals generated by models, behavior, and neurons (Badwan et al., 2019;

410   Chen et al., 2019; Dror et al., 2001; Fitzgerald and Clark, 2015; Leonhardt et al., 2016; Salazar-

411   Gatzimas et al., 2018; Straw et al., 2008). We therefore sought to investigate the performance of

412 the T4 synaptic model in natural motion processing. To do so, we presented it with rigidly-

413 translating scenes from a database of natural images (see **Appendix A, Figure 5A**) (Meyer et al.,

414 2014) (Badwan et al., 2019; Chen et al., 2019; Fitzgerald and Clark, 2015; Meyer et al., 2014;

415 Salazar-Gatzimas et al., 2018). Though the structure and properties of inputs to T5 cells are

416 known to differ from the inputs to T4 (Serbe et al., 2016; Shinomiya et al., 2019), to make an

417 OFF-edge selective channel we created a 'T5' model by simply inverting the ON/OFF selectivity

418 of the inputs to our T4 synaptic model. This is intended merely to be an OFF-selective channel

419 for the purposes of comparing T4 and potential T5 cell responses. The resulting four channels

420 displayed strongly direction-selective average responses to translating natural scenes (**Figure**

421 **5B**).

422

423 Measured responses of T4 and T5 cells to translating natural scenes are decorrelated, so that only

424 one channel is active at once (Salazar-Gatzimas et al., 2018). The synaptic models of T4 and

425 'T5' also generated highly decorrelated responses, with the coactivation matrix of the four

426 channels being nearly diagonal (**Figure 5C**). Such decorrelated parallel channels may provide a

427 convenient representation of motion signals (Salazar-Gatzimas et al., 2018).

428

429 **Discussion**

430

431 An anatomically constrained synaptic model suffices to reproduce many, but not all, of the

432 properties of *Drosophila* T4 cells. This model reproduces the direction-opponency, temporal-

433 frequency-tuning, orientation-tuning, and phi/reverse-phi selectivity measured in T4 cells

434 (**Figures 2-4**). When applied to a naturalistic velocity estimation task, it produces decorrelated

435 signals similar to those measured in T4 and T5 neurons (**Figure 5**). However, it fails to

436 reproduce the PD enhancement and fast-timescale tuning observed in T4 cells (**Figures 3-4**).

437 Moreover, though it is sensitive to triplet correlations in its input, it fails to reproduce them on

438 the same timescales as observed in the data (**Figure 4**). In short, this simple synaptic model is

439 sufficient to reproduce several distinct properties of T4 cells, but cannot account for several

440 observations.

441

442   *Minimal models and levels of understanding*

443   Here, we asked whether a minimal synaptic model could qualitatively reproduce features of T4

444   cell responses. The minimal model required no exotic neurotransmitter receptors or interactions,

445   and was based on simple synaptic conductances. The simplifications sufficient to explain

446   different phenomena will depend strongly on the features one seeks to reproduce, and on the

447   desired level of fidelity. However, minimal models are useful precisely because they can be

448   relatively straightforward to analyze.

449

450   Marr famously proposed different levels of understanding neural circuitry, including an

451   algorithmic level and a mechanistic level (Marr and Poggio, 1976). As we drive towards a deeper

452   understanding of the visual motion circuit in the fly, the levels of algorithm and mechanism can

453   appear increasingly blurred. It is hard to define what distinguishes the mechanistic circuit

454   description presented here from a detailed algorithm-level description of the computation.

455   However, it remains important to connect proposed mechanistic models to high-level

456   descriptions of the system such as the HRC. This is because the high-level descriptions of

457   computations provide a level of intuition for the behavior of the system that a more intricate

458   model cannot. Moreover, the HRC explains a wide variety of neural and behavioral data in flies

459   (Borst and Egelhaaf, 1989; Yang and Clandinin, 2018), so an HRC-like algorithm must be a

460   limiting case of any proposed mechanistic model (Potters and Bialek, 1994).

461

462   *Sufficiency of models*

463   Many details of the function of the early visual system were neglected in this model. For

464   instance, the filter shapes in neurons leading into the model T4 cell have been well-characterized

465   (Arenz et al., 2017; Behnia et al., 2014), but this model used simple exponential filters. Lateral

466   inhibition is widely documented in the early fly visual system (Arenz et al., 2017; Freifeld et al.,

467   2013; Meier et al., 2014), but this model used simple Gaussian spatial acceptance functions

468   without lateral inhibition. The synapses that feed into the medulla neurons that synapse onto T4

469   are likely to have complex, nonlinear processing properties (Yang et al., 2016), yet we modelled

470   the entire input pathway as a purely linear filter. The rectifications of neural responses upstream

471   of T4 are imperfect (Behnia et al., 2014; Salazar-Gatzimas et al., 2018), but this model used

472   simple threshold-linear rectifiers. The fly eye possesses neurons that feedback onto earlier stages

16

473   and create reciprocal interactions between neurons (Takemura et al., 2013; Takemura et al.,

474   2017), but this model is entirely feedforward.

475

476   Despite these approximations, the synaptic T4 model presented here is sufficient to qualitatively

477   match a variety of T4 neuron responses. Adding some of these neglected details into a model

478   may make it sufficient to reproduce other features of T4 responses. This provides a method for

479   understanding which details of processing are related to which response features in T4 cells: one

480   may ask how different details of the system affect the sufficiency of a model to reproduce

481   specific downstream response properties. As the field acquires more and more detailed

482   information about the motion detection circuitry, this sort of analysis will be critical to

483   understand the functional role of different properties.

484

485   One might naturally ask whether the synaptic model presented here might be further simplified

486   without sacrificing its ability to account for the response properties of T4 cells. As described in

487   **Appendix C**, a simplified linear-nonlinear cascade (LNLN) representing the numerator of the

488   biophysical nonlinearity can generate some, but not all, of the properties of the full model.

489

490   *Flexibility in extending this minimal synaptic model*

491   In selecting parameter values for this synaptic model, we sought to reproduce only a few

492   properties of T4 cells: a temporal frequency maximum of 1 Hz and a direction-opponent average

493   responses to sinusoid gratings with a temporal frequency of 1 Hz and a spatial wavelength of 45º

494   (**Appendix B**) (Badwan et al., 2019). To capture a larger subset of the measured properties of T4

495   cells, one could optimize the parameters of the model capture many response properties (Deb,

496   2014). Such a solution would provide information about the maximal ability of this synaptic

497   model to reproduce the properties of T4 cells, but it seems unlikely to provide insight into the

498   predictive power of the core features of the model.

499

500   The organization of this model allows for several clear tuning mechanisms. First, the temporal

501   filters could be modified to better match measured filters (**Figure 2**). Second, the degree to

502   which inhibition is shunting or hyperpolarizing can be adjusted by changing the reversal

503   potential of inhibitory currents. This could effectively hide inhibition under some stimuli and

17

504   measurements. Third, it is clear that to better represent preferred direction enhancement, the

505   threshold for the OFF-inhibitory input could be changed (**Figure 3**) (Borst, 2018). This would

506   allow disinhibition of Mi4 to change the gain for the central input.

507

508   In the model analyzed here, we chose all thresholds of the input LN models to be zero. This

509   effectively ignores contrast asymmetries in the natural world (Geisler, 2008), which have been

510   used to understand many functional properties of motion detectors in flies (Chen et al., 2019;

511   Clark et al., 2014; Fitzgerald and Clark, 2015; Fitzgerald et al., 2011; Leonhardt et al., 2016;

512   Salazar-Gatzimas et al., 2018). Changing these thresholds to optimize for natural scene motion

513   estimation might also generate a parameter set that better captures responses to triplet

514   correlations (**Figure 4**) (Fitzgerald and Clark, 2015). In short, the synaptic model presented here

515   is highly flexible and extensible, and uses only simple, known biophysical mechanisms.

516

517   For the sake of simplicity, we have used single delay and non-delay lines in this work (**Figure**

518   **1A**). However, T4 cells receive fast excitatory input at the center of their receptive fields from

519   both Mi1 and Tm3 cells, and delayed OFF inhibitory input offset in the PD from both Mi4 and

520   CT1 cells (Shinomiya et al., 2019; Takemura et al., 2017). Dissecting how information from

521   these parallel channels is used, particularly if it is nonlinearly combined, will be important in

522   developing a full understanding of the direction-selective computation performed by T4 cells.

523

524   *Modelling temporal processing*

525   The model presented here failed to capture some of the fast-timescale tuning measured in T4,

526   including in its responses to pairwise and triplet spatiotemporal correlations (**Figure 4**). In this

527   minimal model, we represented all temporal processing by linear filters. However, the temporal

528   processing upstream of T4 cells involves nonlinear and adaptive mechanisms, which can affect

529   temporal response properties (Howard et al., 1984; Zheng et al., 2006). Thus far, the study of

530   nonlinear mechanisms in the fly visual system has focused on static nonlinear effects such as

531   rectification (Behnia et al., 2014; Yang et al., 2016) and on nonlinear interactions between

532   linearly filtered signals (Borst et al., 2005; Fitzgerald and Clark, 2015). The inclusion of

533   nonlinear effects on the dynamics themselves may be necessary to accurately capture the

534   temporal processing upstream of T4 cells. As a first step towards experimentally understanding

535   adaptation in this circuit, one might characterize the temporal kernels of the inputs to T4 cells

536   with high resolution (Mano et al., 2019; Yang et al., 2016) and study how their properties depend

537   on stimulus statistics and history (Baccus and Meister, 2002; Kim and Rieke, 2001; Rieke,

538   2001). Only a few models have focused on these sorts of changes in processing dynamics (Clark

539   et al., 2013). Though the analysis of dynamic temporal nonlinearities is complex, incorporating

540   them into models may provide insight into how fast timescale tuning of T4 cells arises.

541

542   *A T5 synaptic model*

543   In this work, we used a sign-inverted version of our T4 synaptic model to represent the OFF-

544   edge-selective T5 cells. This representation would correspond to a first-order direction-selective

545   cell that receives OFF excitatory input at the center of its receptive field, delayed OFF inhibitory

546   input offset in its preferred direction, and delayed ON input offset in the null direction. Such a

547   model would correctly predict the selective responses of T5 cells to phi and reverse-phi apparent

548   motion stimuli (Salazar-Gatzimas et al., 2018). However, the functional and anatomical structure

549   of the inputs to T5 cells suggests that it receives only OFF inputs (Serbe et al., 2016; Shinomiya

550   et al., 2019). Somehow, however, signals in T5 cells are sensitive to both contrast increments and

551   decrements (Salazar-Gatzimas et al., 2018; Wienecke et al., 2018). Further study of the physical

552   and functional connectome of the OFF-edge motion pathway, will be required to elucidate how

553   the direction-selective computations in T4 and T5 cells differ.

554

555   *Relationships to mammalian visual systems*

556   The organization of the fly's visual motion detection circuits bear striking similarities to those in

557   mammalian retina in their anatomy, circuitry, and algorithmic processing (Borst and

558   Helmstaedter, 2015; Clark and Demb, 2016; Sanes and Zipursky, 2010). In mammalian retina,

559   the earliest direction-selective signals are generated by starburst amacrine cells (SACs), which

560   are also tuned to ON- and OFF-edges (Euler et al., 2002; Famiglietti Jr, 1983). It appears that

561   SACs may receive inputs that are differentially delayed (Fransen and Borghuis, 2017; Kim et al.,

562   2014), similar to the inputs to T4 cells. It would be interesting to investigate how much SAC

563   phenomenology that mechanism alone could account for, when linked to simple biophysical

564   mechanisms. As in this study, it could provide insight into where the circuit understanding is

565   lacking, especially when complex stimuli are used to probe SAC function (Chen et al., 2016).

566

567   It is notable that the ON-ON-OFF spatial organization of T4 inputs (**Fig. 1A**) is almost identical

568   to a model proposed to explain cortical responses to pairwise correlations (Mo and Koch, 2003).

569   This suggests there may be deep parallels between T4 and T5 and cortical motion processing

570   steps. Models for fly and cortical direction-selectivity have traditionally differed in whether they

571   assume discrete inputs (fly, HRC-like models) or more continuous inputs (cortex, motion-

572   energy-like spatiotemporal filtering). If synaptic interactions are considered, then continuous

573   linear filters cannot be applied, and models must incorporate the discrete receptive fields of the

574   inputs to a cell. It would be interesting to ask how such conductance models fare in predicting

575   cortical responses; the statistical nature of cortical connections make it more difficult to make a

576   general model of this type.

577

578   In this synaptic model of T4 cell function, we have paired known connectivity with measured

579   physiology and simple biophysics to predict many circuit processing properties. This allows us to

580   define where such a model succeeds and where it fails. This represents progress towards the

581   ultimate goal of understanding this circuit at all levels, from utility to algorithm to mechanism.

582

583   **Author contributions**

584   JAZV and DAC conceived of numerical experiments. JAZV performed numerical simulations

585   and analyzed the model. BAB acquired calcium imaging data. JAZV and DAC wrote the paper.
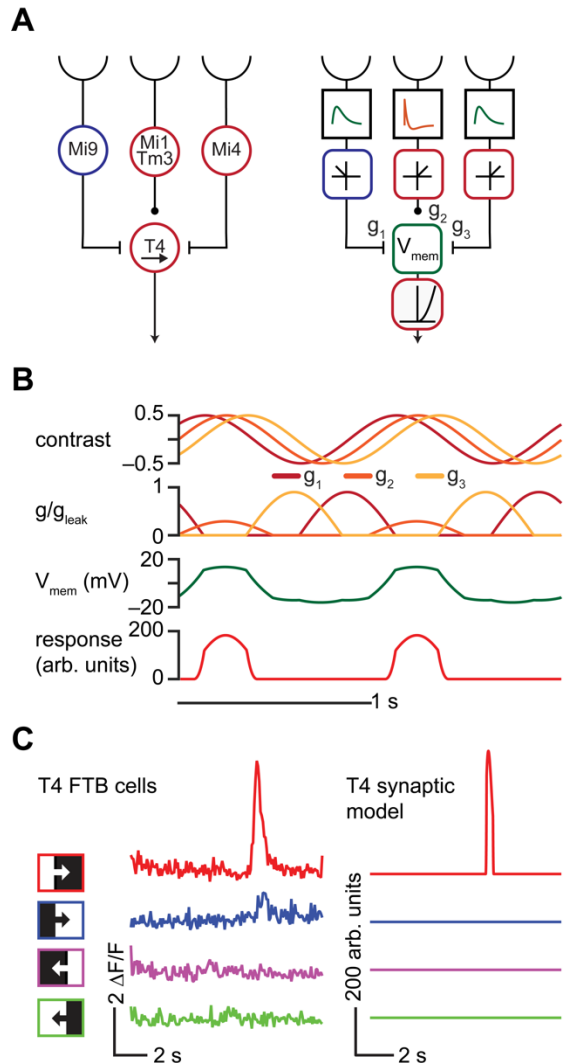
586

587   **Acknowledgements**

Figure Legends

593

Figure 1, Zavatone-Veth et al. (2019)

Figure 1: An anatomically constrained synaptic model for T4 cells.

A. *Left:* Diagram of proposed inputs to *Drosophila* T4 first-order direction-selective cells based on anatomical and physiological measurements. Mi1 and Tm3 cells provide ON excitatory input at the center of the receptive field of each T4 cell, while Mi9 provides delayed OFF inhibitory input offset in the null direction, and Mi4 provides delayed ON inhibitory input offset in the preferred direction. *Right:* Synaptic model based on the anatomical structure shown at left.

21

602 B. Responses of each component of the synaptic model to a 1 Hz, 45º sinusoidal grating

603 drifting in the preferred (rightward) direction. *Top:* Input contrasts to each of the three

604 presynaptic units of the model. *Upper middle:* Conductances of excitatory and inhibitory

605 currents corresponding to each input in response to the sinusoidal stimulus. *Lower*

606 *middle:* Membrane voltage. *Bottom:* Calcium signal.

607 C. *Left:* Responses of T4 cells sensitive to front-to-back (FTB) motion to ON and OFF

608 edges moving FTB and back-to-front (BTF) at 30º/s, measured using two-photon calcium

609 imaging (data from (Salazar-Gatzimas et al., 2016)). *Right:* As at left, but for the T4

610 synaptic model.

611
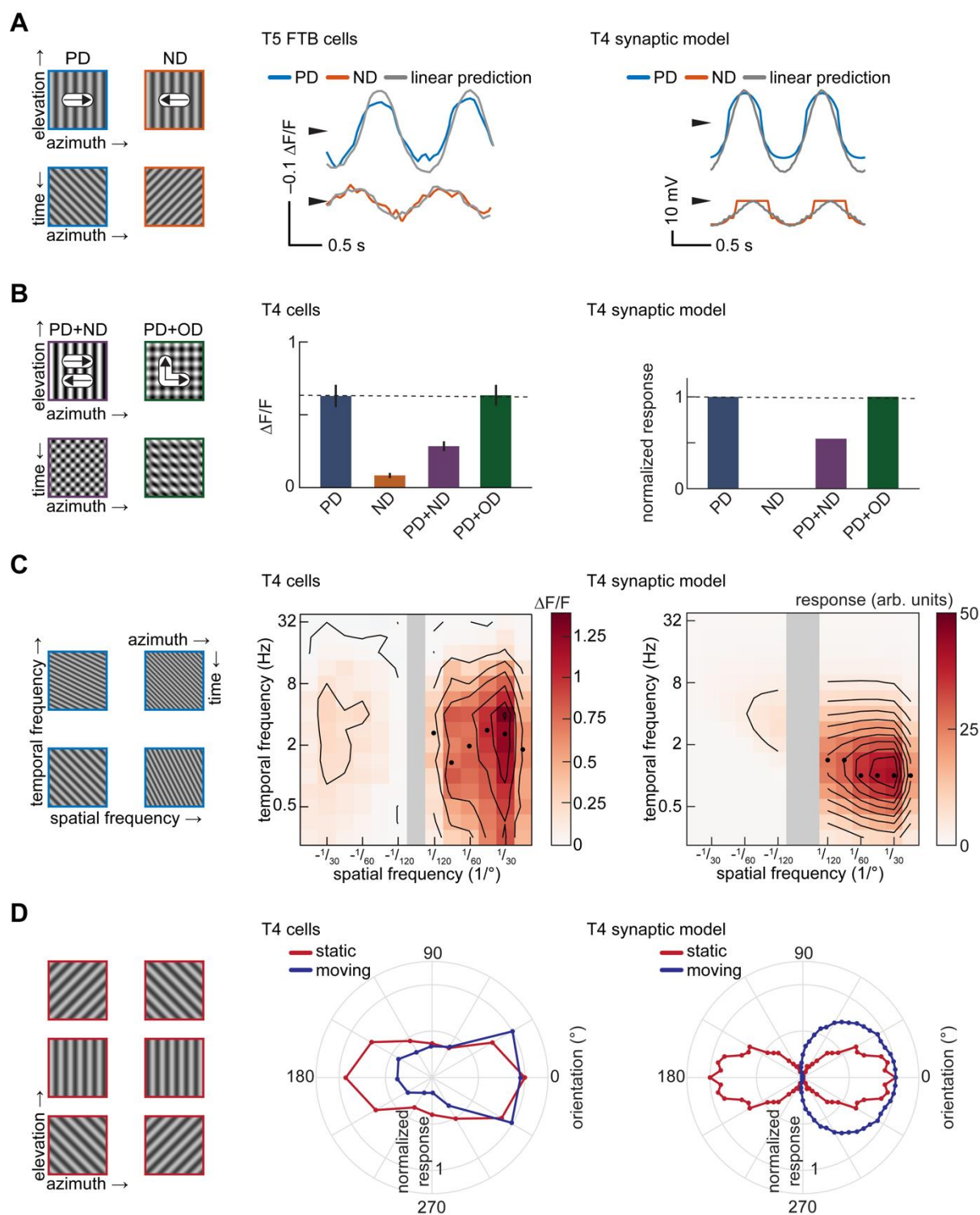
612   **Figure 2**, Zavatone-Veth et al. (2019**)**

613 **Figure 2: The T4 synaptic model reproduces sinusoidal grating responses measured in T4**
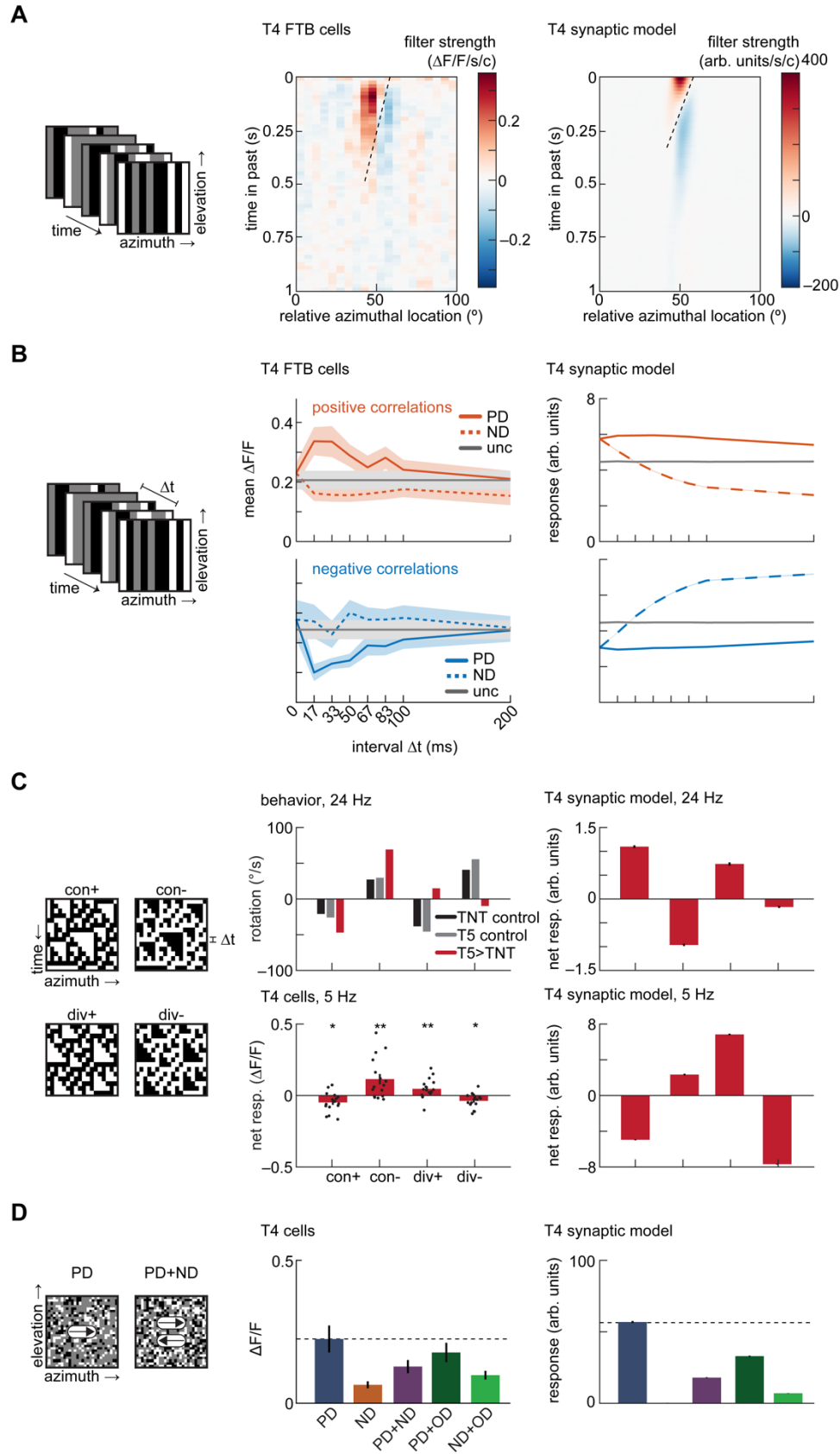
614 **cells.**

615   A. *Left:* Images and kymographs of sinusoid gratings drifting in the preferred (PD) and null

616   (ND) directions. *Center:* Membrane voltage of T5 FTB cells to 1 Hz, 25º drifting gratings

617   compared with linear predictions from contrast-modulated counterphase gratings,

618   measured using voltage indicators (data from (Wienecke et al., 2018)). *Right:* As at

619   center, but for voltage responses of the T4 synaptic model. The model has coefficients of

620   determination for PD and ND of 0.92 and 0.82.

621   B. Mean responses to 1 Hz, 45º sinusoid gratings. *Left:* Images and kymographs of

622   composite sinusoid gratings containing PD and ND motion or PD and orthogonal

623   direction (OD) motion. *Center:* Mean responses of T4 cells to drifting gratings, measured

624   using a calcium indicator (data from (Badwan et al., 2019)). Error bars indicate ±1 SEM.

625   *Right:* As at center, but for calcium responses of the T4 synaptic model.

626   C. Spatiotemporal frequency tuning. *Left:* Kymographs of sinusoid gratings with varying

627   spatiotemporal frequency content. *Center:* Spatiotemporal frequency tuning of T4 cells

628   (data from (Creamer et al., 2018)). Black circles indicate the temporal frequency at which

629   the maximum response at a given spatial frequency is attained. *Right:* As at center, but

630   for the T4 synaptic model.

631   D. Orientation and direction tuning. *Left:* Images of oriented sinusoid gratings. *Center:*

632   Orientation tuning of T4 and T5 cells with static gratings (data from (Fisher et al., 2015))

633   and direction tuning of T4 cells with drifting gratings (data from (Maisak et al., 2013)).

634   The orientation of a static grating is defined by the vector normal to the apparent edges,

635   the same definition as for moving gratings (see **Appendix A**). *Right:* As at center, but for

636   the T4 synaptic model.

637
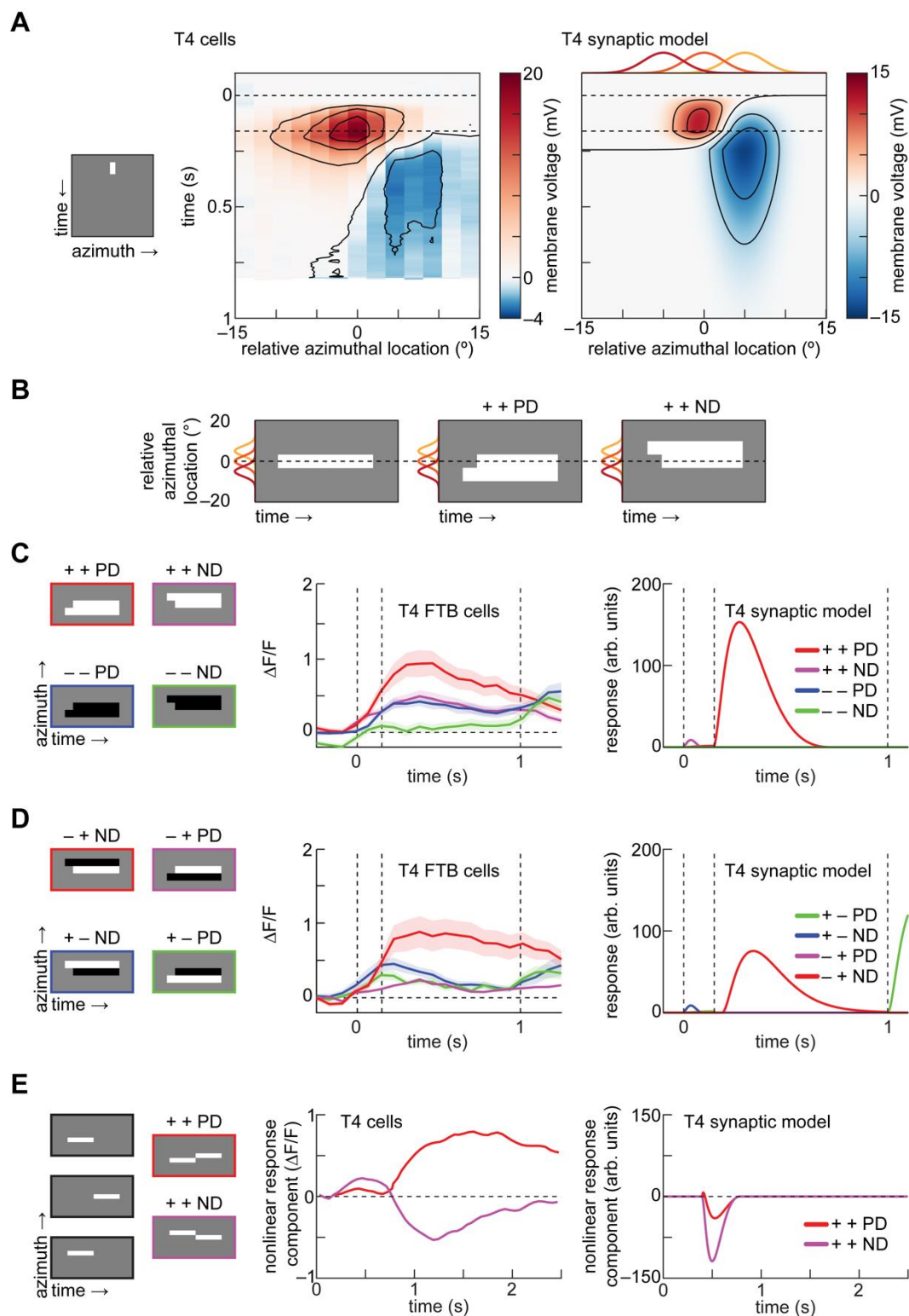
638 **Figure 3**, Zavatone-Veth et al. (2019**)**

25

Figure 3: The T4 synaptic model reproduces the spatial organization and selectivity of apparent motion responses in T4 cells.

A. Responses to a single white bar flashed at different spatial locations. *Left:* Kymograph of 2° white bar presented for 160 ms. *Center:* Membrane voltage of T4 cells to flashed white bars, measured using electrophysiology (data from (Gruntman et al., 2018)). *Right:* As at center, but for the T4 synaptic model. Red, orange, and yellow lines indicate the spatial acceptance functions of the three model inputs.

B. Apparent motion stimuli are aligned such that the lagging bar is located at the center of the receptive field (Salazar-Gatzimas et al., 2018). The leading bar is presented at time zero and lasts for 1 second, and the lagging bar is presented 150 ms later. Each bar subtends 5° of visual angle. Red, orange, and yellow lines indicate the spatial acceptance functions of the three inputs.

C. Responses to phi apparent motion stimuli, aligned as in (B). *Left:* Kymographs of all four possible phi apparent motion stimuli. *Center:* Responses of T4 FTB cells to all four phi apparent motion stimuli, measured using two-photon calcium imaging (data from (Salazar-Gatzimas et al., 2018)). Error patches indicate ±1 SEM. *Right:* As at center, but for the T4 synaptic model.

D. As in (C), but for reverse-phi apparent motion stimuli, in which the sequentially presented bars have opposite contrasts.

E. Assessing PD enhancement and ND suppression. *Left:* Kymographs of linear decomposition of flashed apparent motion stimuli, with 4.5°-wide white bars presented sequentially for 400 ms each. *Center:* Nonlinear response component, defined as the residual of the linear prediction, measured using a calcium indicator (data from (Haag et al., 2016)). *Right:* As at center, but for the T4 synaptic model.

26

Figure 4, Zavatone-Veth et al. (2019**)**

665 **Figure 4: The minimal T4 synaptic model is not sufficient to reproduce the fast-timescale**
666 **tuning of T4 cells.**

667   A. Linear receptive field measurements. *Left:* Schematic depiction of binary, uncorrelated
668   spatiotemporal noise. *Center:* Linear receptive field of T4 FTB cells (data from (Salazar-
669   Gatzimas et al., 2016)). *Right:* As at center, but for the T4 synaptic model.

670   B. Correlation interval receptive field measurements. *Left:* Schematic depiction of ternary
671   noise containing pairwise correlations at a specified interval Δt. *Center:* Responses of T4
672   FTB cells to positive and negative correlations, measured using a calcium indicator (data
673   from (Salazar-Gatzimas et al., 2016)). Error bars indicate ± 1 SEM. *Right:* As at center,
674   but for the T4 synaptic model. Error patches, which are barely visible, indicate 95%
675   confidence intervals of the mean, which is variable due to the stochastic stimulus.

676   C. Triplet correlation sensitivity. *Left:* Kymographs of three-point glider stimuli containing
677   positive and negative triplet correlations. *Center top:* Turning behavioral responses to
678   three-point gliders updated at 24 Hz of flies with the synaptic outputs of T5 cells silenced
679   (data from (Leonhardt et al., 2016)). Positive rotations correspond to the direction of the
680   displacement of the spatial mean location of each triplet. *Center bottom:* Net responses of
681   T4 cells to three-point gliders updated at 5 Hz, measured using a calcium indicator (see
682   **Methods**). Asterisks indicate that median net response differs from zero at the $p < 0.05$
683   (*) or $p < 0.01$ (**) level by a Wilcoxon signed-rank test with N = 16 flies. Exact p-
684   values are p = 0.0174, 0.0061, 0.0097, and 0.0131 for con+, con-, div+, and div-,
685   respectively. Error bars indicate ± 1 SEM over flies, and black circles indicate individual
686   per-fly means. *Right:* As at center, but for the T4 synaptic model. Error bars indicate 95%
687   confidence intervals of the mean.

688   D. Responses to rigidly translating stimuli with stochastic checkerboard patterns. *Left:*
689   Images of random checkerboard stimuli. *Center:* Mean responses of T4 cells to
690   checkerboard stimuli translating at 100º/s, measured using a calcium indicator (data from
691   (Badwan et al., 2019)). Error bars indicate ± 1 SEM. *Right:* As at center, but for the T4
692   synaptic model. Error bars indicate 95% confidence intervals of the mean.

693
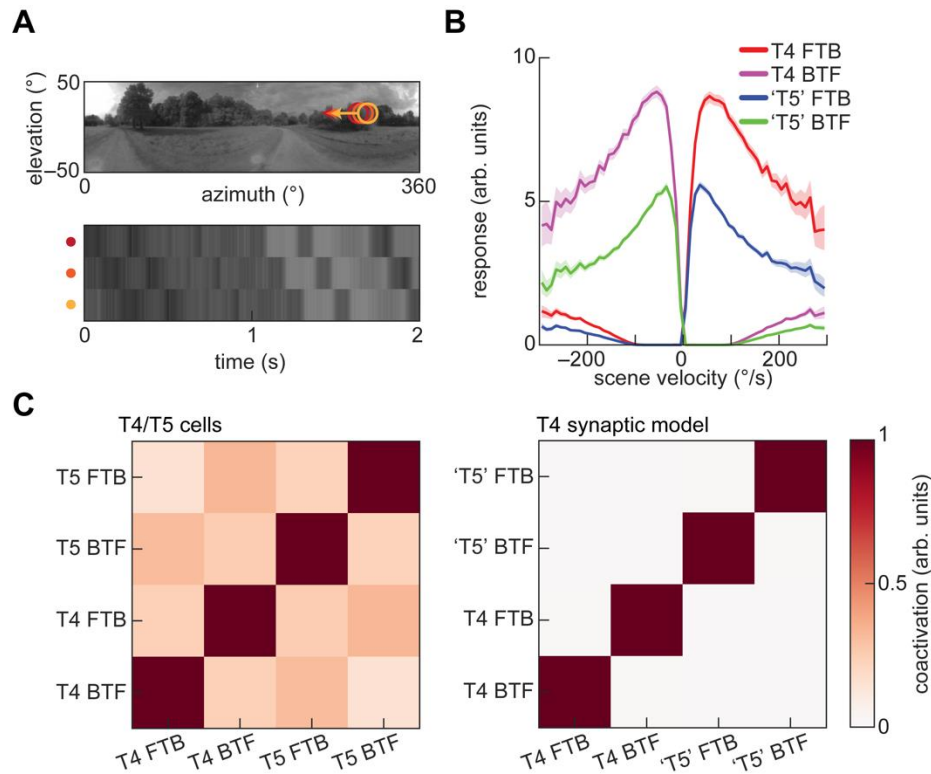
694   **Figure 5**, Zavatone-Veth et al. (2019**)**

695   **Figure 5: The T4 synaptic model generates decorrelated signals in response to naturalistic**

696   **motion.**

697   A. A rigidly rotating panoramic natural scene, with three spatially offset input signals as a

698   function of time.

699   B. Average responses of the T4 synaptic model and a 'T5' variant to naturalistic motion

700   constructed by rigidly translating natural scenes at a variety of velocities. Error patches

701   indicate 95% confidence intervals of the mean. 'T5' cells were constructed by sign-

702   inverting the inputs to the minimal T4 synaptic model.

703   C. Decorrelation of channels with naturalistic motion. *Left:* Coactivation matrix of T4 and

704   T5 cells in response to rigidly translating natural scenes (data from (Salazar-Gatzimas et

705   al., 2018)). *Right:* As at left, but for the T4 synaptic model and 'T5' variant. Coactivation

706   was computed for an ensemble of (image, velocity) pairs, in which the velocity was

707   chosen from a Gaussian distribution with zero mean and 100°/s standard deviation.

708

709   **Appendix A: Visual stimuli used in simulations and imaging experiments**

710

711   In this appendix, we describe in detail all stimuli used in this work.

712

713   *ON and OFF edges (Figure 1)*

714   ON and OFF edges were constructed by placing white (respectively black) edges on a gray

715   background. All edges translated at 30º/s.

716

717   *Sinusoid grating stimuli (Figures 1 and 2)*

718   Sinusoid grating stimuli were constructed as in (Badwan et al., 2019; Creamer et al., 2018;

719   Maisak et al., 2013). Briefly, rightward- and leftward-drifting gratings were constructed as

720

721    $$c(t,x) = c_0 \sin(\omega t \mp \kappa x)$$

722

723   where c_0 is the input contrast, ω is the temporal frequency in units of radians per second, κ is the

724   spatial frequency in units of radians per degree, and the negative sign is taken for rightward-

725   drifting gratings. To assess whether our model is temporal-frequency-tuned, we computed the

726   fraction of the total variance in a spatiotemporal frequency sweep of its responses accounted for

727   by a separable approximation resulting from its singular value decomposition (Creamer et al.,

728   2018). Counterphase gratings were constructed as

729

730    $$c(t,x) = c_0 \sin(\omega t + \kappa x + \phi_1) + c_0 \sin(\omega t - \kappa x + \phi_2)$$

731

732   where ϕ_1 and ϕ_2 are uniformly sampled phase offsets, over which we average in all analyses.

733   Gratings containing preferred- and orthogonal-direction motion were constructed as

734

735    $$c(t,x) = c_0 \sin(\omega t + \kappa x + \phi_1) + c_0 \sin(\omega t + \phi_2)$$

736

737   The linearity analysis in Figure 2A was applied to T5 cells (Wienecke et al., 2018), following a

738   previously developed protocol (Jagadeesh et al., 1993). This analysis relies upon the fact that a

739   drifting sinusoid grating may be decomposed into a sum of counterphase gratings as

30

740

741
$$c(t,x) = c_0 \sin(\omega t \mp \kappa x) = \frac{c_0}{4} \sum_{n=0}^{7} \sin\left(\omega t + \frac{n\pi}{8} \mp \frac{\pi}{2}\right) \sin\left(\kappa x \pm \frac{n\pi}{8}\right)$$

742

743   Therefore, if a system is linear, its scaled, summed response of a linear system to counterphase

744   gratings with these phase shifts will be equal to its response to the corresponding drifting grating.

745   By comparing the linear prediction of the drifting grating response to the actual response, one

746   may assess a system's linearity.

747

748   To assess the orientation- and directional-tuning of the model with sinusoid gratings in Figure

749   2D, we defined a two-dimensional grating

750

751
$$c(t,x,y) = c_0 \sin\bigl(\omega t - \kappa(x \cos\theta + y \sin\theta)\bigr)$$

752

753   where the angle θ defines its orientation. In this analysis, we assume that the ring of detectors is

754   located at $y = 0$, and that the Gaussian spatial filter is symmetric in x and y. Static gratings were

755   formed by setting $\omega = 0$. We note that our convention for the orientation of a static grating

756   differs from the original manuscript (Fisher et al., 2015); we define the orientation as the angle

757   between the normal to the apparent edge and the preferred direction rather than the angular

758   position of the edge itself. Therefore, in our convention the preferred orientations and directions

759   align.

760

761   *Apparent motion stimuli (Figure 3)*

762   Single-bar stimuli were constructed as previously published (Gruntman et al., 2018; Salazar-

763   Gatzimas et al., 2018). Briefly, 5º (respectively 2º) black or white bars were placed on a gray

764   background, and presented for one second (respectively 160 ms) to match (Salazar-Gatzimas et

765   al., 2018) (respectively (Gruntman et al., 2018)). Bar pair apparent motion stimuli were

766   constructed as in (Salazar-Gatzimas et al., 2018). Briefly, 5º black or white bars were placed on a

767   gray background and presented for one second. To create apparent motion, a second black or

768   white bar was added 150 ms after the onset of the first bar at a neighboring spatial location.

769   Responses to these bar pair apparent motion stimuli were aligned such that the location of the

31

770   lagging bar matched the location of peak single-bar responses, as in (Salazar-Gatzimas et al.,

771   2018). Flashed apparent motion stimuli were constructed similarly to those presented to T4 and

772   T5 cells in (Gruntman et al., 2018; Haag et al., 2016). Briefly, 4.5º white bars were placed on a

773   gray background and were presented for 400 ms in sequential spatial positions.

774

775   *Noise stimuli and linear receptive field extraction (Figure 4)*

776   As previously published (Salazar-Gatzimas et al., 2016), we extracted linear receptive fields

777   from responses to uncorrelated binary stimuli composed of 5º black or white bars, updated at 60

778   Hz. We estimated the linear receptive field from these responses using reverse correlation

779   (Chichilnisky, 2001). Ternary noise stimuli with pairwise correlations were constructed as in

780   (Salazar-Gatzimas et al., 2016). Briefly, the contrast of the correlated noise stimulus was given

781   as

782

783
$$c(t,x) = \frac{1}{2}\big(B(t,x) \pm B(t + \delta t, x + \delta x)\big)$$

784

785   where $B(t,x)$ is an uncorrelated binary stimulus composed of 5º black or white bars, and

786   addition (respectively subtraction) generates positive (respectively negative) correlations. The

787   stimulus was updated at a fixed rate, and the temporal offset δt was taken to be one cycle, with

788   its sign determining whether the stimulus was oriented in the preferred or null direction. The

789   spatial offset δx was fixed to be one bar width. As shown in (Salazar-Gatzimas et al., 2016), the

790   autocorrelation function of this stimulus, with spacetime discretized by the bar width and

791   sampling rate, is

792

793
$$\langle c(t,x)c(t+\tau,x+\rho)\rangle = \frac{1}{2}\delta_{\tau,0}\delta_{\rho,0} + \frac{1}{4}\big(\delta_{\tau,\delta t}\delta_{\rho,\delta x} + \delta_{\tau,-\delta t}\delta_{\rho,-\delta x}\big)$$

794

795   where $\delta_{i,j}$ is the Kronecker delta.

796

797   *Three-point glider stimuli (Figure 4)*

798   As in previous studies (Clark et al., 2014; Fitzgerald and Clark, 2015), we constructed three-

799   point glider stimuli following (Hu and Victor, 2010). Briefly, these binary stimuli enforce

800   correlations over space and time among triplets of pixels. Three-point gliders may be categorized

801   into four types: converging gliders with positive parity (con+), converging gliders with negative

802   parity (con-), diverging gliders with positive parity (div+), and diverging gliders with negative

803   parity (div-). Letting ρ be the pixel spacing and δ be the frame duration (the inverse of the

804   update rate), the update rules for each of the four three-point glider types are (see kymographs in

805   **Figure 4**):

806

807
$$c_{\mathrm{con+}}(t,x)c_{\mathrm{con+}}(t,x+\rho)c_{\mathrm{con+}}(t+\delta,x+\rho) = +1$$

808
$$c_{\mathrm{con-}}(t,x)c_{\mathrm{con-}}(t,x+\rho)c_{\mathrm{con-}}(t+\delta,x+\rho) = -1$$

809
$$c_{\mathrm{div+}}(t,x)c_{\mathrm{div+}}(t+\delta,x)c_{\mathrm{div+}}(t+\delta,x+\rho) = +1$$

810
$$c_{\mathrm{div-}}(t,x)c_{\mathrm{div-}}(t+\delta,x)c_{\mathrm{div-}}(t+\delta,x+\rho) = -1$$

811

812   The direction of the displacement of the spatial mean location of each triplet is inverted by

813   inverting the sign of the pixel spacing. Starting from an initial seed state, the values of each pixel

814   at each timepoint are determined by these update rules using the surrounding pixels' values. As

815   we simulate the full 360º of visual space, we use periodic boundary conditions to avoid

816   undetermined edge pixel values. As in previous studies (Clark et al., 2014; Fitzgerald and Clark,

817   2015; Leonhardt et al., 2016), the pixel spacing was taken to be 5º in both imaging experiments

818   and numerical simulations. In imaging experiments, visual stimuli were generated and presented

819   as described in previous studies (Badwan et al., 2019).

820

821   *Random checkerboard stimuli (Figure 4)*

822   Random checkerboard stimuli were constructed as in (Badwan et al., 2019). Briefly, 5º black or

823   white bars were placed at random with a density of 40% on a gray background. The resulting

824   checkerboards were then rigidly translated at a velocity of 100º/s. When combining rightward-

825   and leftward-moving stimuli, summation was defined such that two white bars summed to white,

826   two black bars summed to black, and one white and one black bar summed to gray. Therefore,

827   the contrast of the composite stimulus matched that of the individual components, though its

828   density rose to 64%.

829

830   *Natural scene stimuli (Figure 5)*

831   Following prior work (Chen et al., 2019; Clark et al., 2014; Fitzgerald and Clark, 2015), we

832   generated a left-right symmetric ensemble of natural scenes by drawing independent row and

833   column samples from the database gathered by (Meyer et al., 2014). In this ensemble, scenes

834   were rigidly-translated at velocities sampled from a Gaussian distribution with a standard

835   deviation of 100º/s, which roughly matches typical rotational velocities of walking flies

836   (DeAngelis et al., 2019; Katsov and Clandinin, 2008). To convert the scenes to contrast signals,

837   we spatially filtered each image with the photoreceptor kernel to generate blurred images I_{blur},

838   and then used a Gaussian kernel with a standard deviation of 20º to estimate locally-averaged

839   images I_{mean} (Chen et al., 2019). The contrast signal was then defined as

840

841
$$c(x, y) := \frac{I_{\mathrm{blur}}(x, y) - I_{\mathrm{mean}}(x, y)}{I_{\mathrm{mean}}(x, y)}$$

842

843   As in previous studies of coactivation (Salazar-Gatzimas et al., 2018), the coactivations in Figure

844   5C were computed as normalized inner products of response timeseries. For all analyses in

845   Figure 5, we used an ensemble with 10^6 elements.

846

847 **Appendix B: Parameter value selection**

848

849 In this appendix, we briefly describe how we selected values of the weighting parameters

850 $g_{\mathrm{exc}}/g_{\mathrm{leak}}$ and $g_{\mathrm{inh}}/g_{\mathrm{leak}}$. We evaluated the model solely based on its ability to produce

851 direction-opponent average responses to 1 Hz, 45º sinusoid gratings similar to those measured in

852 T4 cells (Badwan et al., 2019). To do so, we considered the direction selectivity index and

853 analogous indices of direction-opponency and orthogonal direction enhancement, defined as

854

855
$$\mathrm{DSI} := \frac{r(PD) - r(PD)}{r(PD) + r(PD)},$$

856

857
$$I_{\mathrm{PD+ND}} := \frac{r(PD + ND) - r(PD)}{r(PD + ND) + r(PD)},$$

858 and

859
$$I_{\mathrm{PD+OD}} := \frac{r(PD + OD) - r(PD)}{r(PD + OD) + r(PD)}$$

860

861 As shown in **Figure B1**, there exists a broad region of parameter space for which the model

862 produces responses with a similar degree of direction-opponency to that measured in T4 cells

863 without significant PD+OD enhancement. We therefore made a simple choice of round-number

864 values within that region.

865
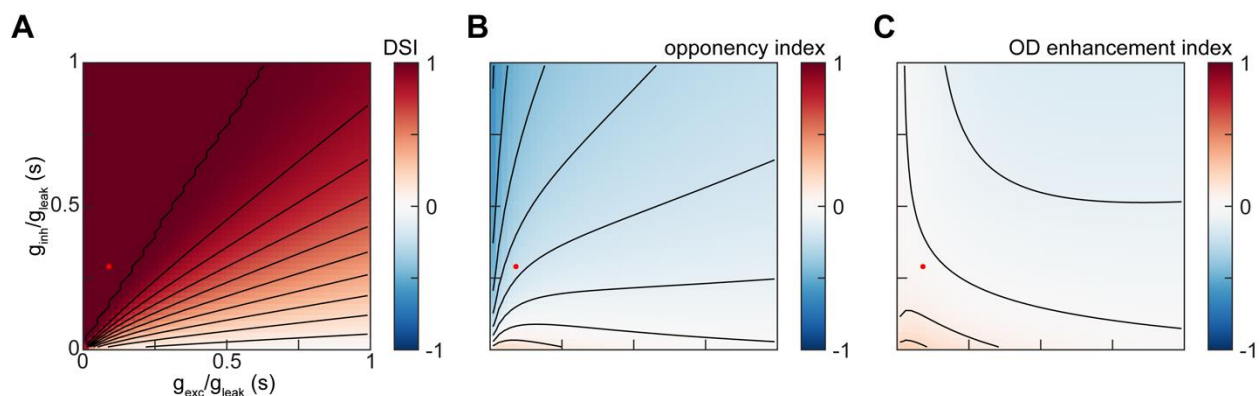
866 **Appendix Figure B1**, Zavatone-Veth et al. (2019**)**

867 **Appendix Figure B1: Sweeping the parameters of the T4 synaptic model.**

35

868   A. The direction-selectivity index of the T4 synaptic model's responses to drifting sinusoid

869   gratings as a function of $g_{\mathrm{exc}}/g_{\mathrm{leak}}$ and $g_{\mathrm{inh}}/g_{\mathrm{leak}}$. Red dot indicates the selected values

870   of $g_{\mathrm{exc}}/g_{\mathrm{leak}} = 0.1$ and $g_{\mathrm{inh}}/g_{\mathrm{leak}} = 0.3$.

871   B. As in (A), but for the opponency index.

872   C. As in (A), but for the OD enhancement index.

873

Appendix C: LNLN cascade factorization of the T4 synaptic model

In this appendix, we show how our T4 synaptic model may be factorized as a product of linear-nonlinear-linear-nonlinear (LNLN) cascades representing the numerator and denominator of the biophysical nonlinearity. The response C of the full model at each point in spacetime is given in terms of the filtered contrast signal s as

$$C = R^2 \left(\frac{\tilde{g}_1 E_{\text{inh}} + \tilde{g}_2 E_{\text{exc}} + \tilde{g}_3 E_{\text{inh}}}{1 + \tilde{g}_1 + \tilde{g}_2 + \tilde{g}_3} \right)$$

where we have defined $\tilde{g}_i := g_i / g_{\text{leak}}$ for brevity. Noting that the denominator of this expression is always positive, we may re-express the response as

$$C = \frac{R^2 (\tilde{g}_1 E_{\text{inh}} + \tilde{g}_2 E_{\text{exc}} + \tilde{g}_3 E_{\text{inh}})}{(1 + \tilde{g}_1 + \tilde{g}_2 + \tilde{g}_3)^2}$$

hence the full EMD model admits a factorization into a product of LNLN models as

$$C(t, x) = N(t, x) \, D(t, x)$$

where

$$N(t, x) := R^2 (\tilde{g}_1 E_{\text{inh}} + \tilde{g}_2 E_{\text{exc}} + \tilde{g}_3 E_{\text{inh}})$$

and

$$D(t, x) := (1 + \tilde{g}_1 + \tilde{g}_2 + \tilde{g}_3)^{-2}$$

which is bounded as $D(t, x) \leq 1$. Because $D(t, x) \leq 1$, $C(t, x) \leq N(t, x)$.

The denominator LNLN cascade D is the result of applying a convex function (x^{-2} for $x > 0$) to a non-negative linear combination of LN models with convex nonlinearities. Therefore, it cannot

37

903   generate direction-opponent (DO) average responses to sinusoid gratings. The proof of this

904   proposition is a minor extension of our previous results on LNLN models with continuously-

905   differentiable convex nonlinearities and non-negative secondary linear filters (Badwan et al.,

906   2019). We define the soft ramp function

907

908 $$R_\beta(x) := \beta^{-1} \log(1 + \exp(\beta x))$$

909

910   which is a continuously differentiable, monotone increasing, non-negative, and convex function

911   of x for all positive β. As $\beta \to \infty$, $R_\beta(x) \to R(x)$ pointwise. By continuity, defining $D_\beta(t, x)$

912   using R_β, we have $0 \leq D_\beta(t, x) \to D(t, x) \leq 1$ as $\beta \to \infty$. We denote the nonlinear functional

913   corresponding to the spacetime average of $D_\beta(t, x)$ for some input stimulus f as $D_\beta[f]$. As we

914   have the integrable constant dominating function 1, by the Lebesgue dominated convergence

915   theorem we have $0 \leq D_\beta[f] \to D[f] \leq 1$ as $\beta \to \infty$ (Stein and Shakarchi, 2009). By the result of

916   (Badwan et al., 2019), we know that $D_\beta[PD + ND] \geq D_\beta[PD]$ and $D_\beta[PD + ND] \geq D_\beta[ND]$,

917   where $D_\beta[PD]$, $D_\beta[ND]$, and $D_\beta[PD + ND]$ are the average responses to PD, ND, and PD+ND

918   sinusoid gratings, respectively. As these inequalities hold pointwise for all positive β, by taking

919    $\beta \to \infty$ we may obtain $D[PD + ND] \geq D[PD]$ and $D[PD + ND] \geq D[ND]$. Therefore, the

920   denominator LNLN cascade cannot generate DO average responses to sinusoid gratings.

921

922   However, as the numerator LNLN model is the result of applying a convex function to a non-

923   convex linear combination of LN models with convex nonlinearities, we cannot analytically

924   exclude the possibility that it could generate DO average responses to sinusoid gratings using the

925   results of (Badwan et al., 2019). In fact, numerical simulation shows that it can generate DO

926   average responses to sinusoid gratings, though it generates strong PD+OD enhancement (**Figure**

927   **C1**). It also generates DO responses over a smaller region in spatiotemporal frequency space

928   than the full model. If one replaced the infinitely sharp ramp functions with more biophysically

929   plausible soft rectifiers, the numerator LNLN cascade would be well-approximated for small

930   input contrasts by a LN model with a quadratic nonlinearity. Therefore, it could not generate DO

931   average responses for sufficiently small input contrasts. However, even in the limit in which both

932   the numerator and denominator are represented as LN models with quadratic nonlinearities, the

38

933   full model could likely generate DO average responses. In particular, this limiting construction

934   would resemble a type of adaptive gain model which was previously shown to generate DO

935   average responses (Badwan et al., 2019).

936
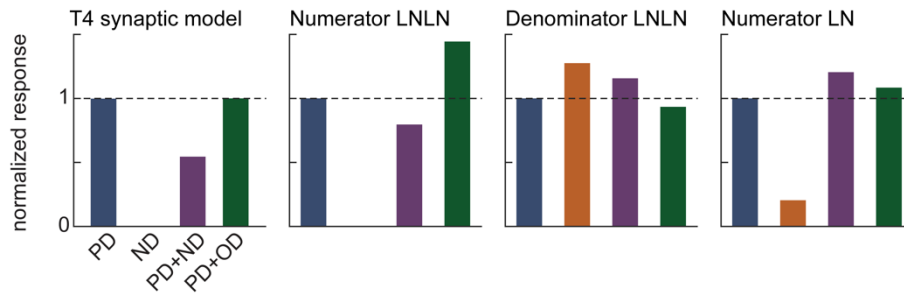
937   **Appendix Figure C1**, Zavatone-Veth et al. (2019**)**

938   **Appendix Figure C1: Sinusoid grating responses of different components of the LNLN**

939   **factorization.**

940   *From left to right:* Average responses of the full T4 synaptic model, the numerator LNLN

941   cascade, the denominator LNLN cascade, and the numerator LN cascade to 1 Hz, 45º sinusoid

942   gratings. All responses are normalized by the response of the given component to a grating

943   drifting in the PD of the full model.

944

39

References

Adelson, E., and Bergen, J. (1985). Spatiotemporal energy models for the perception of motion. JOSA A *2*, 284-299.

Anstis, S. (1970). Phi movement as a subtraction process. Vision Res *10*, 1411-1430.

Arenz, A., Drews, M.S., Richter, F.G., Ammer, G., and Borst, A. (2017). The temporal tuning of the Drosophila motion detectors is determined by the dynamics of their input elements. Curr Biol *27*, 929-944.

Baccus, S., and Meister, M. (2002). Fast and slow contrast adaptation in retinal circuitry. Neuron *36*, 909-919.

Badwan, B.A., Creamer, M.S., Zavatone-Veth, J.A., and Clark, D.A. (2019). Dynamic nonlinearities enable direction opponency in Drosophila elementary motion detectors. Nat Neurosci *22*, 1318-1326.

Barlow, H., and Levick, W.R. (1965). The mechanism of directionally selective units in rabbit's retina. J Physiol *178*, 477.

Behnia, R., Clark, D.A., Carter, A.G., Clandinin, T.R., and Desplan, C. (2014). Processing properties of ON and OFF pathways for Drosophila motion detection. Nature *512*, 427-430.

Borst, A. (2018). A biophysical mechanism for preferred direction enhancement in fly motion vision. PLoS Comp Biol *14*, e1006240.

Borst, A., and Egelhaaf, M. (1989). Principles of visual motion detection. Trends Neurosci *12*, 297-306.

Borst, A., Flanagin, V.L., and Sompolinsky, H. (2005). Adaptation without parameter change: Dynamic gain control in motion detection. Proc Natl Acad Sci USA *102*, 6172-6176.

Borst, A., and Helmstaedter, M. (2015). Common circuit design in fly and mammalian motion vision. Nat Neurosci *18*, 1067-1076.

Brainard, D.H. (1997). The psychophysics toolbox. Spatial vision *10*, 433-436.

Chen, J., Mandel, H.B., Fitzgerald, J.E., and Clark, D.A. (2019). Asymmetric ON-OFF processing of visual motion cancels variability induced by the structure of natural scenes. eLife *8*, e47579.

Chen, Q., Pei, Z., Koren, D., and Wei, W. (2016). Stimulus-dependent recruitment of lateral inhibition underlies retinal direction selectivity. Elife *5*, e21053.

Chichilnisky, E. (2001). A simple white noise analysis of neuronal light responses. Network: Comput Neural Syst *12*, 199-213.

978 Clark, D.A., Benichou, R., Meister, M., and da Silveira, R.A. (2013). Dynamical Adaptation in
979 Photoreceptors. PLoS Comp Biol *9*, e1003289.

980 Clark, D.A., Bursztyn, L., Horowitz, M.A., Schnitzer, M.J., and Clandinin, T.R. (2011). Defining
981 the computational structure of the motion detector in Drosophila. Neuron *70*, 1165-1177.

982 Clark, D.A., and Demb, J.B. (2016). Parallel computations in insect and mammalian visual
983 motion processing. Curr Biol *26*, R1062-R1072.

984 Clark, D.A., Fitzgerald, J.E., Ales, J.M., Gohl, D.M., Silies, M., Norcia, A.M., and Clandinin,
985 T.R. (2014). Flies and humans share a motion estimation strategy that exploits natural scene
986 statistics. Nat Neurosci *17*, 296-303.

987 Creamer, M.S., Mano, O., and Clark, D.A. (2018). Visual Control of Walking Speed in
988 Drosophila. Neuron *100*, 1460-1473.

989 Creamer, M.S., Mano, O., Tanaka, R., and Clark, D.A. (2019). A flexible geometry for
990 panoramic visual and optogenetic stimulation during behavior and physiology. J Neurosci
991 Methods *323*, 48-55.

992 Dayan, P., and Abbott, L.F. (2001). Theoretical neuroscience (Cambridge, MA: MIT Press).

993 DeAngelis, B.D., Zavatone-Veth, J.A., and Clark, D.A. (2019). The manifold structure of limb
994 coordination in walking Drosophila. eLife *8*, e46409.

995 Deb, K. (2014). Multi-objective optimization. In Search methodologies (Springer), pp. 403-449.

996 Dror, R.O., O'Carroll, D.C., and Laughlin, S.B. (2001). Accuracy of velocity estimation by
997 Reichardt correlators. JOSA A *18*, 241-252.

998 Efron, B. (1987). Better bootstrap confidence intervals. Journal of the American statistical
999 Association *82*, 171-185.

1000 Eichner, H., Joesch, M., Schnell, B., Reiff, D.F., and Borst, A. (2011). Internal structure of the
1001 fly elementary motion detector. Neuron *70*, 1155-1164.

1002 Euler, T., Detwiler, P.B., and Denk, W. (2002). Directionally selective calcium signals in
1003 dendrites of starburst amacrine cells. Nature *418*, 845-852.

1004 Famiglietti Jr, E.V. (1983). On and off pathways through amacrine cells in mammalian retina:
1005 the synaptic connections of "starburst" amacrine cells. Vision Res *23*, 1265-1279.

1006 Fisher, Y.E., Silies, M., and Clandinin, T.R. (2015). Orientation selectivity sharpens motion
1007 detection in Drosophila. Neuron *88*, 390-402.

1008 Fitzgerald, J.E., and Clark, D.A. (2015). Nonlinear circuits for naturalistic visual motion
1009 estimation. eLife, e09123.

1010   Fitzgerald, J.E., Katsov, A.Y., Clandinin, T.R., and Schnitzer, M.J. (2011). Symmetries in
1011   stimulus statistics shape the form of visual motion estimators. Proc Natl Acad Sci USA *108*,
1012   12909-12914.

1013   Fransen, J.W., and Borghuis, B.G. (2017). Temporally Diverse Excitation Generates Direction-
1014   Selective Responses in ON-and OFF-Type Retinal Starburst Amacrine Cells. Cell Rep *18*, 1356-
1015   1365.

1016   Freifeld, L., Clark, D.A., Schnitzer, M.J., Horowitz, M.A., and Clandinin, T.R. (2013).
1017   GABAergic lateral interactions tune the early stages of visual processing in Drosophila. Neuron
1018   *78*, 1075-1089.

1019   Geisler, W.S. (2008). Visual perception and the statistical properties of natural scenes. Annu Rev
1020   Psychol *59*, 167-192.

1021   Gruntman, E., Romani, S., and Reiser, M.B. (2018). Simple integration of fast excitation and
1022   offset, delayed inhibition computes directional selectivity in Drosophila. Nat Neurosci, 1.

1023   Haag, J., Arenz, A., Serbe, E., Gabbiani, F., and Borst, A. (2016). Complementary mechanisms
1024   create direction selectivity in the fly. Elife *5*.

1025   Hassenstein, B., and Reichardt, W. (1956). Systemtheoretische Analyse der Zeit-, Reihenfolgen-
1026   und Vorzeichenauswertung bei der Bewegungsperzeption des Rüsselkäfers Chlorophanus. Zeits
1027   Naturforsch *11*, 513–524.

1028   Hollander, M., Wolfe, D.A., and Chicken, E. (2013). Nonparametric statistical methods, Vol 751
1029   (John Wiley & Sons).

1030   Howard, J., Dubs, A., and Payne, R. (1984). The dynamics of phototransduction in insects. J
1031   Comp Physiol A *154*, 707-718.

1032   Hu, Q., and Victor, J.D. (2010). A set of high-order spatiotemporal stimuli that elicit motion and
1033   reverse-phi percepts. J Vis *10*.

1034   Jagadeesh, B., Wheat, H.S., and Ferster, D. (1993). Linearity of summation of synaptic potentials
1035   underlying direction selectivity in simple cells of the cat visual cortex. Science *262*, 1901-1904.

1036   Joesch, M., Schnell, B., Raghu, S., Reiff, D., and Borst, A. (2010). ON and OFF pathways in
1037   Drosophila motion vision. Nature *468*, 300-304.

1038   Kato, S., Xu, Y., Cho, C.E., Abbott, L., and Bargmann, C.I. (2014). Temporal responses of C.
1039   elegans chemosensory neurons are preserved in behavioral dynamics. Neuron *81*, 616-628.

1040   Katsov, A., and Clandinin, T. (2008). Motion processing streams in Drosophila are behaviorally
1041   specialized. Neuron *59*, 322-335.

Kim, J.S., Greene, M.J., Zlateski, A., Lee, K., Richardson, M., Turaga, S.C., Purcaro, M., Balkam, M., Robinson, A., and Behabadi, B.F. (2014). Space-time wiring specificity supports direction selectivity in the retina. Nature *509*, 331-336.

Kim, K., and Rieke, F. (2001). Temporal contrast adaptation in the input and output signals of salamander retinal ganglion cells. J Neurosci *21*, 287-299.

Kleiner, M., Brainard, D., Pelli, D., Ingling, A., Murray, R., and Broussard, C. (2007). What's new in Psychtoolbox-3. Perception *36*, 1.

Kunze, P. (1961). Untersuchung des Bewegungssehens fixiert fliegender Bienen. Zeitschrift für vergleichende Physiologie *44*, 656-684.

Leong, J.C.S., Esch, J.J., Poole, B., Ganguli, S., and Clandinin, T.R. (2016). Direction selectivity in Drosophila emerges from preferred-direction enhancement and null-direction suppression. J Neurosci *36*, 8078-8092.

Leonhardt, A., Ammer, G., Meier, M., Serbe, E., Bahl, A., and Borst, A. (2016). Asymmetry of Drosophila ON and OFF motion detectors enhances real-world velocity estimation. Nat Neurosci *19*, 706–715.

Maisak, M.S., Haag, J., Ammer, G., Serbe, E., Meier, M., Leonhardt, A., Schilling, T., Bahl, A., Rubin, G.M., Nern, A.*, et al.* (2013). A directional tuning map of Drosophila elementary motion detectors. Nature *500*, 212-216.

Mano, O., Matulis, C.A., Creamer, M.S., Salazar-Gatzimas, E., Chen, J., Zavatone-Veth, J.A., and Clark, D.A. (2019). Using slow frame rate imaging to extract fast receptive fields. Nature Communications *10*, 4979.

Marr, D., and Poggio, T. (1976). From understanding computation to understanding neural circuitry. In AI Memo (Massachussetts Institute of Technology).

Meier, M., Serbe, E., Maisak, M.S., Haag, J., Dickson, B.J., and Borst, A. (2014). Neural circuit components of the Drosophila OFF motion vision pathway. Curr Biol *24*, 385-392.

Meyer, H.G., Schwegmann, A., Lindemann, J.P., and Egelhaaf, M. (2014). Panoramic high dynamic range images in diverse environments.

Mo, C.-H., and Koch, C. (2003). Modeling reverse-phi motion-selective neurons in cortex: double synaptic-veto mechanism. Neural Comput *15*, 735-759.

Pelli, D.G. (1997). The VideoToolbox software for visual psychophysics: Transforming numbers into movies. Spatial vision *10*, 437-442.

Potters, M., and Bialek, W. (1994). Statistical mechanics and visual signal processing. J Physique *4*, 1755-1775.

1075   Priebe, N.J., Lisberger, S.G., and Movshon, J.A. (2006). Tuning for spatiotemporal frequency
1076   and speed in directionally selective neurons of macaque striate cortex. J Neurosci *26*, 2941-2950.

1077   Qian, N., Andersen, R.A., and Adelson, E.H. (1994). Transparent motion perception as detection
1078   of unbalanced motion signals. I. Psychophysics. J Neurosci *14*, 7357-7366.

1079   Rieke, F. (2001). Temporal contrast adaptation in salamander bipolar cells. J Neurosci *21*, 9445-
1080   9454.

1081   Salazar-Gatzimas, E., Agrochao, M., Fitzgerald, J.E., and Clark, D.A. (2018). The Neuronal
1082   Basis of an Illusory Motion Percept Is Explained by Decorrelation of Parallel Motion Pathways.
1083   Curr Biol *28*, 3748-3762. e3748.

1084   Salazar-Gatzimas, E., Chen, J., Creamer, M.S., Mano, O., Mandel, H.B., Matulis, C.A.,
1085   Pottackal, J., and Clark, D.A. (2016). Direct measurement of correlation responses in Drosophila
1086   elementary motion detectors reveals fast timescale tuning. Neuron *92*, 227-239.

1087   Sanes, J.R., and Zipursky, S.L. (2010). Design principles of insect and vertebrate visual systems.
1088   Neuron *66*, 15.

1089   Serbe, E., Meier, M., Leonhardt, A., and Borst, A. (2016). Comprehensive characterization of the
1090   major presynaptic elements to the Drosophila OFF motion detector. Neuron *89*, 829-841.

1091   Shinomiya, K., Huang, G., Lu, Z., Parag, T., Xu, C.S., Aniceto, R., Ansari, N., Cheatham, N.,
1092   Lauchie, S., and Neace, E. (2019). Comparisons between the ON-and OFF-edge motion
1093   pathways in the Drosophila brain. eLife *8*, e40025.

1094   Stavenga, D. (2003). Angular and spectral sensitivity of fly photoreceptors. II. Dependence on
1095   facet lens F-number and rhabdomere type in Drosophila. Journal of Comparative Physiology A:
1096   Neuroethology, Sensory, Neural, and Behavioral Physiology *189*, 189-202.

1097   Stein, E.M., and Shakarchi, R. (2009). Real analysis: measure theory, integration, and Hilbert
1098   spaces (Princeton University Press).

1099   Straw, A.D., Rainsford, T., and O'Carroll, D.C. (2008). Contrast sensitivity of insect motion
1100   detectors to natural images. J Vis *8*, 32-32.

1101   Strother, J.A., Wu, S.-T., Wong, A.M., Nern, A., Rogers, E.M., Le, J.Q., Rubin, G.M., and
1102   Reiser, M.B. (2017). The emergence of directional selectivity in the visual motion pathway of
1103   Drosophila. Neuron *94*, 168-182. e110.

1104   Takemura, S.-y., Bharioke, A., Lu, Z., Nern, A., Vitaladevuni, S., Rivlin, P.K., Katz, W.T.,
1105   Olbris, D.J., Plaza, S.M., and Winston, P. (2013). A visual motion detection circuit suggested by
1106   Drosophila connectomics. Nature *500*, 175-181.

1107   Takemura, S.-y., Nern, A., Chklovskii, D.B., Scheffer, L.K., Rubin, G.M., and Meinertzhagen,
1108   I.A. (2017). The comprehensive connectome of a neural substrate for 'ON'motion detection in
1109   Drosophila. Elife *6*.

1110   Torre, V., and Poggio, T. (1978). A synaptic mechanism possibly underlying directional
1111   selectivity to motion. Proc R Soc Lond B *202*, 409-416.

1112   Wienecke, C.F., Leong, J.C., and Clandinin, T.R. (2018). Linear Summation Underlies Direction
1113   Selectivity in Drosophila. Neuron.

1114   Yang, H.H., and Clandinin, T.R. (2018). Elementary motion detection in Drosophila: algorithms
1115   and mechanisms. Ann Rev Vis Sci *4*, 143-163.

1116   Yang, H.H., St-Pierre, F., Sun, X., Ding, X., Lin, M.Z., and Clandinin, T.R. (2016). Subcellular
1117   imaging of voltage and calcium signals reveals neural processing in vivo. Cell *166*, 245–257.

1118   Zheng, L., de Polavieja, G.G., Wolfram, V., Asyali, M.H., Hardie, R.C., and Juusola, M. (2006).
1119   Feedback network controls photoreceptor output at the layer of first visual synapses in
1120   Drosophila. J Gen Physiol *127*, 495-510.
1121